

Using open data to rapidly benchmark biomolecular simulations: Phospholipid internal dynamics

Hanne S. Antila,[†] Tiago Ferreira,[‡] Matti Javanainen,[¶] O. H. Samuli Ollila,[§] and Markus S. Miettinen^{*,†}

[†]*Department of Theory and Bio-Systems, Max Planck Institute of Colloids and Interfaces, 14424 Potsdam, Germany*

[‡]*NMR Group — Institute for Physics, Martin-Luther University Halle–Wittenberg, 06120 Halle (Saale), Germany*

[¶]*Add Matti to author list?*

[§]*Institute of Biotechnology, University of Helsinki, 00014 Helsinki, Finland*

E-mail: markus.miettinen@iki.fi

Abstract

Molecular dynamics (MD) simulations are widely used to study the atomistic structure and dynamics of biomembranes. It remains unknown, however, how well the conformational dynamics observed in MD simulations correspond to those occurring in real life phospholipids. The accuracy of such time scales in MD can be assessed by comparing against the effective correlation times τ_e of the C-H bonds measured in nuclear magnetic resonance experiments (J. Chem. Phys. 142 044905 (2015)).

Here, we extend this previous analysis by considering carefully the error estimation of MD-determined τ_e , and analyze the conformational dynamics of phospholipids as produced by several commonly used MD models (force fields). None of the tested force fields reproduced all the effective correlation times within experimental error, much like they do not provide accurate conformational ensemble (J. Phys. Chem. B 119 15075 (2015)). However, the dynamics observed in CHARMM36 and Slipids were more realistic than those seen in the Amber Lipid14, OPLS-based MacRog, and GROMOS-based Berger force fields, where dynamics of the

glycerol backbone was unrealistically slow.

1 Introduction

Ever since the conception of Protein Data Bank (PDB)^{1,2} and GenBank,^{3,4} open access to standardised and searchable pools of experimental data has revolutionized scientific research. Constantly growing and mostly improving in fidelity due to collaborative effort,^{5–8} the now hundreds of databanks⁹ fuel the data-driven development of biomolecular structure determination,¹⁰ refinement,¹¹ prediction,¹² and design¹³ approaches, as well as development of drugs,^{14,15} materials,^{16,17} and more.^{18,19} It is clear that open data enables scientific progress that is far beyond the resources of a single research group or institute. Consequently, the call for public availability and conservation of data has extended to molecular dynamics (MD) simulation trajectories of biomolecules,^{20–22} and the discussion on how and by whom such databanks for dynamic structures would be set up is currently active.^{23–26} While no general MD trajectory databank currently operates, individual databanks are accepting contributions on nucleic acid,²⁷ protein/DNA/RNA,²⁸ cyclodex-

trin,²⁹ G-protein-coupled receptor,³⁰ and lipid bilayer³¹ simulations.

Since 2013, the NMRlipids Project (nmrlipids.blogspot.fi) has promoted a fully open collaboration approach, where the whole scientific research process—from initial ideas and discussions to analysis methods, data, and publications—is all the time publicly available.³² While its main focus has been on conformational ensembles of different lipid headgroups and on ion binding to lipid membranes,^{32–34} the NMRlipids Project has also built a databank³¹ containing hundreds of atomistic MD trajectories of lipid bilayers (zenodo.org/communities/nmrlipids), indexed at nmrlipids.fi.

MD databanks are expected to be particularly relevant for disordered biomolecules, such as biological lipids composing cellular membranes or intrinsically disordered proteins. These, in contrast to folded proteins or DNA strands, cannot be meaningfully described by the coordinates of a single structure alone. Realistic MD simulations, however, can provide the complete conformational ensemble and dynamics of such molecules, as well as enable studies of their biological functions in complex biomolecular assemblies. Unfortunately, the current MD force fields largely fail to capture the conformational ensembles of lipid headgroups and disordered proteins.^{32,34–37} Therefore, before they can be used to draw conclusions, the quality of MD simulations must always be carefully assessed against structurally sensitive experiments. For lipid bilayers, such evaluation is possible against NMR and scattering data.³⁸

Here we demonstrate the use of a pre-existing, publicly available set of MD trajectories to rapidly evaluate the fidelity of phospholipid conformational dynamics in state-of-the-art force fields. The speed at which individual molecules sample their conformational ensemble is traditionally used to assess if a given MD simulation has converged. Going beyond such practicalities, realistic dynamics are particularly desired for the intuitive interpretation of NMR experiments sensitive to molecular motions,³⁹ as well as to understand the dynamics of biological processes where molecular defor-

mations play a rate-limiting role, such as membrane fusion.⁴⁰ The here presented comprehensive comparison of dynamics between experiments and different MD models at various biologically relevant compositions and conditions is thus likely to facilitate the development of increasingly realistic phospholipid force fields.

Above all, our results demonstrate the power of publicly available MD trajectories in creating new knowledge at a lowered computational cost and high potential for automation. We believe that this paves the way for novel applications of MD trajectory databanks, as well as underlines their usefulness—not only for lipid membranes, but for all biomolecular systems.

2 Methods

2.1 Evaluation of conformational dynamics of lipids against NMR data

We analyze lipid dynamics based on two quantities available from published ¹³C-NMR experiments:^{41–43} The effective C–H bond correlation time τ_e and the spin-lattice relaxation rate R_1 , both directly quantifiable from atomistic MD simulations. The τ_e are effectively an average over all the time scales relevant for the lipid internal dynamics, and respond intuitively to changes in these: Increasing τ_e always signals some type of slowdown in the C–H bond dynamics.⁴¹ The R_1 rates (or the corresponding T_1 times) have been traditionally used to assess both the conformational dynamics of lipids in experiments^{44–48} and the dynamics produced by MD models in simulations.^{44,46,47,49} In contrast to τ_e , the R_1 are sensitive to processes within a rather narrow time scale window set by the magnet frequency, and changes in R_1 are not intuitively related to changes in process speeds: A decrease in R_1 tells that the amount of processes in the sensitive time window decreases, but not if the corresponding processes become faster or slower.

¹³C NMR experiments investigating lipid conformational dynamics take advantage of the fact that the relaxation of ¹³C magnetization

dominantly happens via the dipolar coupling of the carbon with the magnetic moments of the protons bound to it, with the symmetry axis of the interaction aligning with the C–H bond. The spectral density depicting the ^{13}C relaxation rates (at frequency ω) is expressed as

$$j(\omega) = 2 \int_0^\infty \cos(\omega\tau)g(\tau)d\tau, \quad (1)$$

which is the Fourier transformation of the C–H bond second order autocorrelation function at time τ

$$g(\tau) = \langle P_2(\vec{\mu}(t) \cdot \vec{\mu}(t + \tau)) \rangle, \quad (2)$$

where $\vec{\mu}(t)$ is the unit vector in the direction of the C–H bond at time t and P_2 is the second order Legendre polynomial. The angular brackets depict averaging over time. The autocorrelation function can be expressed as the product of two functions

$$g(\tau) = g_f(\tau)g_s(\tau), \quad (3)$$

where $g_f(\tau)$ characterizes fast decays owing to, for example, the molecular rotations, and $g_s(\tau)$ describes slow decays that originate from, e.g., lipid diffusion. The two components, along with the oscillation due to magic angle spinning at the $\sim\text{kHz}$ region, are depicted in Fig. 1. Correlation time of 4.2 ms has been estimated for multilamellar POPC samples at 300 K for the slow modes, whereas in liquid crystalline lipid bilayers the faster $g_f(\tau)$ decays to a plateau value S_{CH}^2 within a few hundred nanoseconds.⁴¹ The C–H bond order parameters

$$S_{\text{CH}} = \frac{1}{2} \langle 3 \cos^2 \theta(t) - 1 \rangle, \quad (4)$$

where $\theta(t)$ is the angle between the bond and the bilayer normal, are measured in NMR experiments from this plateau. As S_{CH} describes the conformational ensemble of the molecule, the fast-decaying component of the rotational correlation function intuitively depicts the time needed to sample these conformations. The characteristic time can be quantified via the ef-

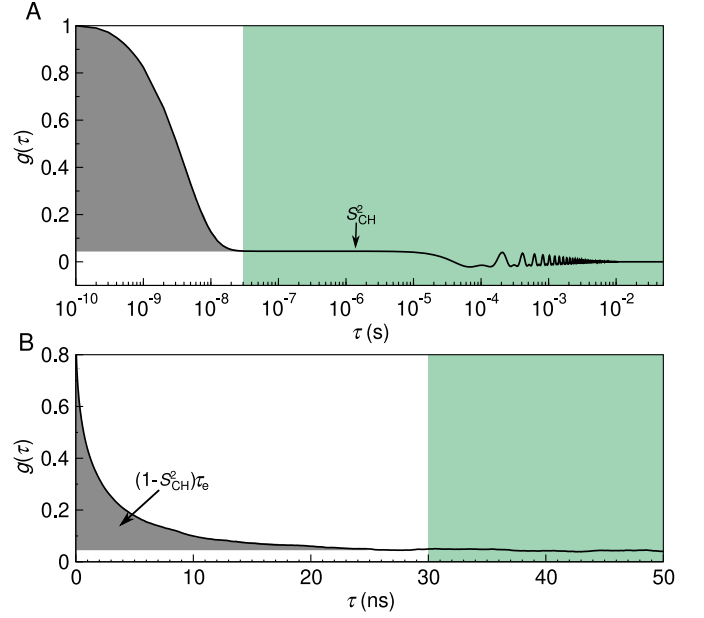


Figure 1: The autocorrelation function $g(\tau)$ a) The fast mode (white background) and the slow mode (shaded green) of the correlation function along with the oscillation owing to magic angle spinning. The fast mode decays to a plateau quantifying the S_{CH} while the slow mode gives the final descent to zero. b) Illustration of typical C–H bond autocorrelation function obtained from a MD simulation. The gray area under the curve gives a way of quantifying the τ_e .

fective correlation time

$$\tau_e = \int_0^\infty \frac{g_f(\tau) - S_{\text{CH}}^2}{1 - S_{\text{CH}}^2} d\tau. \quad (5)$$

The integrand can be viewed as a reduced and normalized correlation function

$$g'_f(\tau) = \frac{g_f(\tau) - S_{\text{CH}}^2}{1 - S_{\text{CH}}^2}. \quad (6)$$

That is, τ_e is defined as the area under $g'_f(\tau)$, as graphically depicted in Fig. 1b. **1.Maybe also add 1C that explicitly shows g'_f ?** It is easily seen that in the presence of more long-lived correlations τ_e grows, signaling that more time is needed for full conformational sampling.

The spin-lattice relaxation rate R_1 defines the time-scale on which ^{13}C longitudinal magnetiza-

tion equilibrates. It is defined as

$$R_1 = \frac{d_{\text{CH}}^2 N_{\text{H}}}{20} [j(\omega_{\text{H}} - \omega_{\text{C}}) + 3j(\omega_{\text{C}}) + 6j(\omega_{\text{H}} + \omega_{\text{C}})], \quad (7)$$

where N_{H} is the number of bound hydrogens, ω_{H} and ω_{C} are the Larmor frequencies for ^1H and ^{13}C , and d_{CH} is the rigid dipolar coupling constant. For the methylene bond, $d_{\text{CH}}/2\pi$ approximately equals to -22 kHz. **2.why there is a minus sign above?**

The dependency of R_1 on the spectral densities j at the Larmor frequencies means that the R_1 value depicts the relative amounts of relaxation processes with time-scales near the inverses of these frequencies. Since the Larmor frequencies depend on the field strength used in the NMR measurements, this typically makes R_1 sensitive to ~ 1 – 10 ns time-scales. Importantly, a change in R_1 thus indicates a difference in the relative amounts of processes within the detection window, and therefore does not give information on the modulation of the total sampling rate.

2.2 Experimental data acquisition and analysis

All the experimental quantities were collected from the literature **3.Except are they, or mostly from Tiago and re-analysed from raw data?** sources referred at the respective figures **4.How to refer to experimental data from Tiago?**.

2.3 Simulational data acquisition and analysis

The simulation trajectories used in this work were collected from the Zenodo repository (zenodo.org) with majority of the data originating from the NMRlipids Project^{32,33} (nmrlipids.blogspot.fi). Table 1 details, with references to the trajectory files, the simulations of pure POPC bilayers at/near room temperature and at full hydration, whereas Table 2 lists simulations including cholesterol; Table 3 simulations with varying hydration; and Table 4 at increasing NaCl concentration.

Table 1: Analyzed simulations of POPC lipid bilayers at standard conditions.

force field	N_1^a	N_w^b	$T^c(\text{K})$	$t_{\text{anal}}^d(\text{ns})$	files ^e
Berger-POPC-07 ⁵⁰	128	7290	298	50	[51]
CHARMM36 ⁵²	128	5120	303	140	[53]
	34	1020	300	140	[54]
MacRog ⁵⁵	128	6400	310	200	[56]
Lipid14 ⁵⁷	72	2234	303	50	[58]
Slipids ⁵⁹	200	9000	310	500	[60]
ECC ⁶¹	128	6400	300	300	[62]

^aNumber of POPC molecules.

^bNumber of water molecules.

^cSimulation temperature.

^dTrajectory length used for analysis.

^eReference for the openly available simulation files.

Additional computational details for each of the simulations are available at the cited Zenodo entry.

Table 2: Analyzed simulations of cholesterol-containing POPC bilayers.

force field POPC/cholesterol	c_{chol}^a	N_{chol}^b	N_1^c	N_w^d	$T^e(\text{K})$	$t_{\text{anal}}^f(\text{ns})$	files ^g
Berger-POPC-07 ⁵⁰	0%	0	128	7290	298	50	[51]
/Höltje-CHOL-13 ^{63,64}	50%	64	64	10314	298	60	[65]
CHARMM36 ⁵²	0%	0	128	5120	303	140	[53]
/CHARMM36 ⁶⁶	50%	80	80	4496	303	200	[67]
MacRog ⁵⁵	0%	0	128	6400	310	200	[56]
/MacRog ⁵⁵	50%	64	64	6400	310	200	[56]
Slipids ⁵⁹	0%	0	200	9000	310	500	[60]
/Slipids ⁶⁸	50%	200	200	18000	310	500	[60]

^aBilayer cholesterol content (mol %).

^bNumber of cholesterol molecules.

^cNumber of POPC molecules.

^dNumber of water molecules.

^eSimulation temperature.

^fTrajectory length used for analysis.

^gReference for the openly available simulation files.

The simulation data were analyzed using in-house scripts. These are available on GitHub[?] along with a Python notebook outlining an example analysis run. After downloading the necessary files from Zenodo, the trajectory was processed with Gromacs `gmx trjconv` to make the molecules whole. The C–H bond order parameters S_{CH} , see Eq. (4), were then calculated with the `calcOrderParameters.py`[?] script that uses the MDanalysis[?] Python library. The C–H bond correlation functions $g(\tau)$, see Eq. (2), were calculated with Gromacs5.1.4[?] `gmx rotacf`; note that on simula-

Table 3: Analyzed simulations of lipid bilayers under varying hydration level.

force field	lipid	$n_{w/l}$ ^a	N_l ^b	N_w ^c	T^d (K)	t_{anal}^e (ns)	files ^f
Berger-POPC-07 ⁵⁰	POPC	57	128	7290	298	50	[51]
Berger-DLPC-13 ⁶⁹	DLPC ^g	24	72	1728	300	80	[70]
	DLPC ^g	16	72	1152	300	80	[71]
	DLPC ^g	12	72	864	300	80	[72]
Berger-POPC-07 ⁵⁰	POPC	7	128	896	298	60	[73]
Berger-DLPC-13 ⁶⁹	DLPC ^g	4	72	288	300	80	[74]
CHARMM36 ⁵²	POPC	40	128	5120	303	140	[53]
	POPC	15	72	1080	303	20	[75]
	POPC	7	72	504	303	20	[76]
MacRog ⁵⁵	POPC	50	288	14400	310	40	[77]
	POPC	15	288	4320	310	100	[77]
	POPC	10	288	2880	310	100	[77]

^aWater/lipid molar ratio.

^bNumber of lipid molecules.

^cNumber of water molecules.

^dSimulation temperature.

^eTrajectory length used for analysis.

^fReference for the openly available simulation files.

^g1,2-didodecanoyl-sn-glycero-3-phosphocholine.

5. The data points here do not match those in Fig. 5B.

MacRog in Fig. 5B: 50, 25, 10, 5 w/l, and C36 in

Fig. 5B: 40, 31, 15, 7 w/l.

6. The t_{anal} for MacRog here do not match Ref. 77

(100 ns \rightarrow 50 ns)?

Table 4: Analyzed simulations of POPC lipid bilayers at varying NaCl concentration.

force field POPC/ions	[NaCl] ^a (mM)	N_{Na} ^b	N_l ^c	N_w ^d	T^e (K)	t_{anal}^f (ns)	files ^g
CHARMM36 ⁵² /CHARMM36 ⁷⁸	0	0	128	5120	303	140	[53]
	346	13	72	2085	303	80	[79]
	692	26	72	2085	303	73	[80]
	947	37	72	2168	303	60	[81]
MacRog ⁵⁵ /OPLS ⁸²	0	0	128	6400	310	400	[56]
	103	27	288	14554	310	90	[83]
	207	54	288	14500	310	90	[83]
	311	81	288	14446	310	80	[83]
	416	108	288	14392	310	90	[83]
Slipids ⁵⁹ /AMBER ⁸⁴	0	0	200	9000	310	500	[60]
	130	21	200	9000	310	100	[85]
	999	162	200	9000	310	200	[86]

^aNaCl concentration, calculated as $[\text{NaCl}] = N_{\text{Na}} \times [\text{water}] / N_w$, where $[\text{water}] = 55.5 \text{ M}$.

^bNumber of Na^+ ions, equal to number of Cl^- ions.

^cNumber of POPC molecules.

^dNumber of water molecules.

^eSimulation temperature.

^fTrajectory length used for analysis.

^gReference for the openly available simulation files.

tional (fast) time scales $g = g_s g_f = g_f$. To obtain the g'_f , the S_{CH} were used to normalize the g_f following Eq. (6).

The effective correlation times τ_e were then calculated by integrating $g'_f(\tau)$, see Eqs. (5) and (6), over time from $\tau = 0$ until $\tau = t_0$. Here $t_0 = \min\{t | g'_f(t) = 0\}$, that is, t_0 is the first time point at which g'_f reached zero. If g'_f did not reach zero within $t_{\text{anal}}/2$, the τ_e was not determined, and we report only its upper and lower error estimates.

To quantify the error on τ_e , we first estimate the error on $g'_f(\tau)$, where we account for two sources of uncertainty, $g_f(\tau)$ and S_{CH}^2 . Performing linear error propagation on Eq. (6) gives

$$\Delta g'_f(\tau) = \left| \frac{1}{1 - S_{\text{CH}}^2} \right| \Delta g_f(\tau) + \left| \frac{2(g_f(\tau) - 1) S_{\text{CH}}}{(1 - S_{\text{CH}}^2)^2} \right| \Delta S_{\text{CH}}. \quad (8)$$

Here the ΔS_{CH} was determined as in the NMR-lipids Project:³² as the standard error of the mean of the S_{CH} of all the N_l individual lipids in the system. Similarly, we quantified the error on $g_f(\tau)$ by first determining an individual correlation function $g_f^m(\tau)$ for each lipid m over the whole trajectory, and then obtaining the error estimate $\Delta g_f(\tau)$ as the standard error of the mean over the N_l lipids. Importantly, this gives an uncertainty estimate at each time point τ .

To obtain the lower bound on τ_e , we integrate the function $g'_f(\tau) - \Delta g'_f(\tau)$ over time from $\tau = 0$ until $\tau = t_l$. Here

$$t_l = \min \left\{ \{t | g'_f(t) - \Delta g'_f(t) = 0\}, \frac{t_{\text{anal}}}{2} \right\}. \quad (9)$$

That is, t_l equals the first time point at which the lower error estimate of g'_f reached zero; or $t_l = t_{\text{anal}}/2$, if zero was not reached by that point.

To obtain the upper error estimate on τ_e , we first integrate the function $g'_f(\tau) + \Delta g'_f(\tau)$ over time from $\tau = 0$ until $t_u = \min\{t_0, t_{\text{anal}}/2\}$. Note, however, that this is not yet sufficient, because there could be slow processes that our simulation was not able to see. Although these

would contribute to τ_e with a low weight, their contribution over long times could still add up to a sizable effect on τ_e . That said, it seems feasible to assume (see Fig. 1A) that there are no longer-time contributions to g_f than something that decays with a time constant of 10^{-6} s. We use this as our worst case estimate to assess the upper bound for τ_e , and assume that all the decay from the time point $t_u = \min\{t_0, t_{\text{anal}}/2\}$ onwards comes solely from this slowest process. The additional contribution to the upper bound for τ_e then reads $\Delta g'_f(t_u) \times (\exp(-t_u/10^{-6} \text{ s}) - \exp(-1)) \times 10^{-6} \text{ s}$.

7. Discuss the possibility of skewed error distributions?

The R_1 rates were calculated using Eq. (7). The spectral density $j(\omega)$ was obtained from the normalized correlation function g'_f by fitting it with a sum of $N = 71$ exponentials

$$g'_f(\tau) \approx \sum_{i=1}^N \alpha_i e^{-\tau/\tau_i}, \quad (10)$$

with logarithmically spaced time-scales τ_i ranging from 0.1 ps to 1 μs , and then calculating the spectral density of this fit based on the Fourier transformation⁴¹

$$j(\omega) = 2(1 - S_{\text{CH}}) \sum_{i=1}^N \alpha_i \frac{\tau_i}{1 + \omega^2 \tau_i^2}. \quad (11)$$

The R_1 rate of a given C–H bond was first calculated separately for each lipid m (using Eq. (7) with $N_{\text{H}} = 1$, and $j^m(\omega)$ obtained for the normalized correlation function g_f^m). The resulting N_1 measurements per bond were then assumed independent: Their mean gave the R_1 rate of the bond, and standard error of the mean its uncertainty. The total R_1 rate of a given carbon was obtained as a sum of the R_1 rates of its C–H bonds. When several carbons contribute to the experimental R_1 rate of a carbon segment, the carbon-wise R_1 rates were averaged to obtain the segment-wise R_1 rate. The segment-wise error estimates were obtained by standard error propagation, starting from the uncertainties of the R_1 rates of the C–H bonds.

To gain some qualitative insight on the time scales at which the main contributions to the (headgroup) R_1 rates arise, we also looked at

'cumulative' R_1 rates, $R_1(\tau)$. These contained just those contributions in the sum of Eq. (11) for which $\tau_i < \tau$. Note that here the g'_f averaged over lipids was used; therefore, the 'cumulative' $R_1(\tau \rightarrow \infty)$ does not necessarily have exactly the same numerical value as the actual R_1 .

Finally, we note that the fit of Eq. (10) provides an alternative to estimating τ_e , because

$$\tau_e = \int_0^\infty g'_f(\tau) d\tau \approx \sum_{i=1}^N \alpha_i \tau_i. \quad (12)$$

When the simulation trajectory is not long enough for the correlation function to reach the plateau, integrating g'_f gives a lower bound estimate for τ_e , while the sum of Eq. (12) includes also (some) contribution from the longer-time components via the fitting process. However, in practice the fit is often highly unreliable in depicting the long tails of the correlation function, and thus we chose to quantify τ_e using the area under g'_f , and estimate its uncertainty as detailed above.

3 Results and Discussion

In the following, we discuss phospholipid conformational dynamics in six different MD force fields. We do this first for standard conditions (pure POPC bilayers, full hydration, no salt; see Table 1 for simulation details and Fig. 2 for results) and then proceed to cover a wider range of experimentally, biologically, and computationally relevant conditions. We investigate how the dynamics change when cholesterol is added to the bilayer (Table 2 and Fig. 4), when hydration level is reduced (Table 3 and Fig. 5), and when monovalent salt is added to the solution (Table 4 and Fig. 7).

One should keep in mind that none of the force fields we study produces all the C–H bond order parameters, S_{CH} , within experimental accuracy.³² This means that the structural ensembles simulated do not exactly match the structural ensemble occurring in reality. Consequently, the τ_e times and R_1 rates depict the dynamics of sampling a somewhat different phase space for each model. To this

end, we avoid overly detailed discussion on the models and rather concentrate on common and qualitative trends.

Effective correlation times τ_e at standard conditions.

The left panels of Fig. 2 compare the τ_e obtained for fully hydrated POPC bilayers in experiments (black) and in the six different MD force fields (color).

Qualitatively, every force field captures the general shape of the τ_e profile: Dynamics slows down towards the glycerol backbone in both the headgroup and the tails. Quantitatively, MD has a tendency towards slightly too fast dynamics in the membrane core, but at the water-facing interface MD is typically too slow. CHARMM36 and Slipids show the best overall performance—although the τ_e in Slipids exhibit a qualitatively wrong (decreasing) trend from g_3 to g_1 .

The detected slow glycerol backbone dynamics in MD is consistent with previous results for the Berger model.⁴¹ It also agrees with the insufficient conformational sampling of glycerol backbone torsions observed in 500-ns-long CHARMMc32b2^{87,88} simulations of a DOPC lipid.⁸⁹

Note that the temperature varied across these openly available simulation data. However, it was in no case lower than in the experiment. Were the simulations done at the experimental 298 K, the overestimation of τ_e at the glycerol backbone by MD would get worse as τ_e increases at decreasing temperature—as indicated by the CHARMM36 data covering several temperatures. **8.HA: add new CHARMM36 data to plot**

R_1 rates at standard conditions.

The panels on the right side of Fig. 2 compare experimental and simulated R_1 rates under the same conditions as for the τ_e on the left.

There are certain qualitative features that all force fields predict correctly (for example that g_2 has the smallest R_1 among the glycerol and C9 among the oleoyl double bond segments),

and certain that they all miss (that R_1 rates for the oleoyl segments C8, C10, and C11 are all roughly equal).

Quantitatively, there are a few cases where both R_1 and τ_e (almost) match experiments, suggesting (almost) correct rotational dynamics at all relevant time scales. For example, Slipids performs well at the β and α segments; CHARMM36 for the g_3 , g_2 , C2 and C3; Lipid14 and ECC for the oleoyl double bond; and MacRog for the tail end segments.

Notably, there are also instances where the R_1 comparison distinctly differs from what is seen for τ_e : Some models that do very well for τ_e , do rather poorly for R_1 . Conversely, a matching R_1 can be accompanied by a larger-than-experimental τ_e . To appreciate such differences, recall that in order to capture our experimental R_1 rates (measured at 125 MHz) a force field has to have correct rotational dynamics at the $(2\pi \times 125 \text{ MHz})^{-1} \approx 1 \text{ ns}$ time scale, whereas τ_e reflects all the sub- μs time scales (Fig. 1).

MacRog for the β , α , g_3 , and g_1 segments provides a prominent example where the R_1 rates are well reproduced, but τ_e times systematically overestimated. Such a combination suggests that MD does well at the 1 ns scale, but has too slow long-time dynamics.

The opposite—where τ_e matches experiments, but R_1 does not—is demonstrated by all five all-atom force fields for the γ segment, and by CHARMM36 for β and α . Therein a cancellation of error occurs in τ_e : The wrong dynamics at the 1 ns scale are compensated by wrong dynamics at the other time scales. As CHARMM36 overall performs rather well for both R_1 and τ_e , we proceed to study this shortcoming on the headgroup R_1 rates in some more detail.

Dynamics of headgroup segments in CHARMM36.

Figure 3A zooms in on the headgroup (γ , β , α) segments, whose τ_e were not clearly visible on the scale of Fig. 2. For all three, CHARMM36 matches the experimental τ_e , but overestimates R_1 . No other force field does any better for γ , but for β and α Slipids provides almost perfect

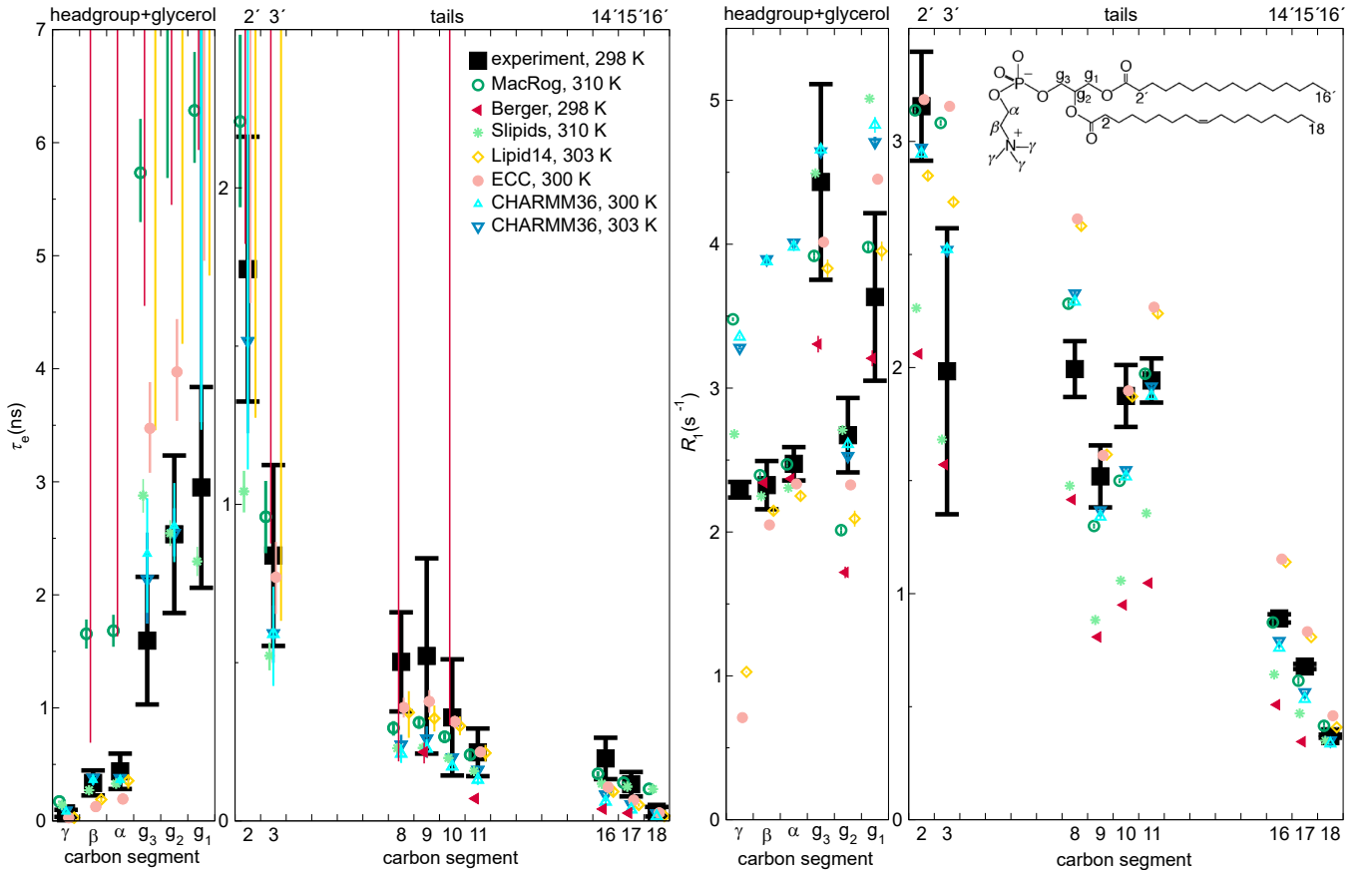


Figure 2: Effective correlation times (τ_e , left panels) and R_1 rates (right panels) in experiments (black) and MD simulations (colored) of POPC bilayers in L_α phase under full hydration. Inset on the right shows the POPC structure and carbon segment labeling. Each plotted value contains contributions from all the hydrogens within its carbon segment; the data for segments 8–11 are only from the sn-2 (oleoyl) chain, whereas the (experimentally non-resolved) contributions of both tails are included for segments 2–3 (2′–3′ in the sn-1 chain) and 16–18 (14′–16′). Simulation data are only shown for the segments for which there exists experimental data. For τ_e , a simulation data point indicates the average over C–H bonds; however, if τ_e could not be determined for all bonds, only the error bar (extending from the mean of the lower to the mean of the upper error estimates) is shown. The Berger data for methyl segments (γ , C18, and C16′) are left out, because the protonation algorithm used to construct the hydrogens post-simulation in united atom models does not preserve the methyl C–H bond dynamics. Table 1 provides further simulation details. Error bars for the experimental values reflect error estimate of XXX.

9.Experimental error estimate changed since the data were originally published; needs to be explained to the reader.

10.How to refer to the experiments? Not really from previous publication because of re-analysis.

dynamics.

To investigate where the differences between force fields arise, we visualize the ‘cumulative’ $R_1(\tau)$ in Fig. 3B. It is obtained, as detailed in Methods, by including in the sum of Eq. (11) only terms with $\tau_i < \tau$. Consequently, at $\tau \rightarrow \infty$ the ‘cumulative’ $R_1(\tau)$ approaches the actual R_1 . Ranges of steepest increase therefore indicate time scales that most strongly con-

tribute to R_1 rates.

Figure 3B shows that for models that overestimate the R_1 rate of γ (MacRog, CHARMM36, and Slipids, see Fig. 3A) the major contribution to R_1 arises at $\tau > 50$ ps, whereas those underestimating the R_1 (Lipid14 and ECC, see Fig. 2) the major contribution comes from $\tau < 50$ ps. This also manifests in the distribution of fitting weights (α_i in Eq. (10)) in Fig. 3C: The earlier

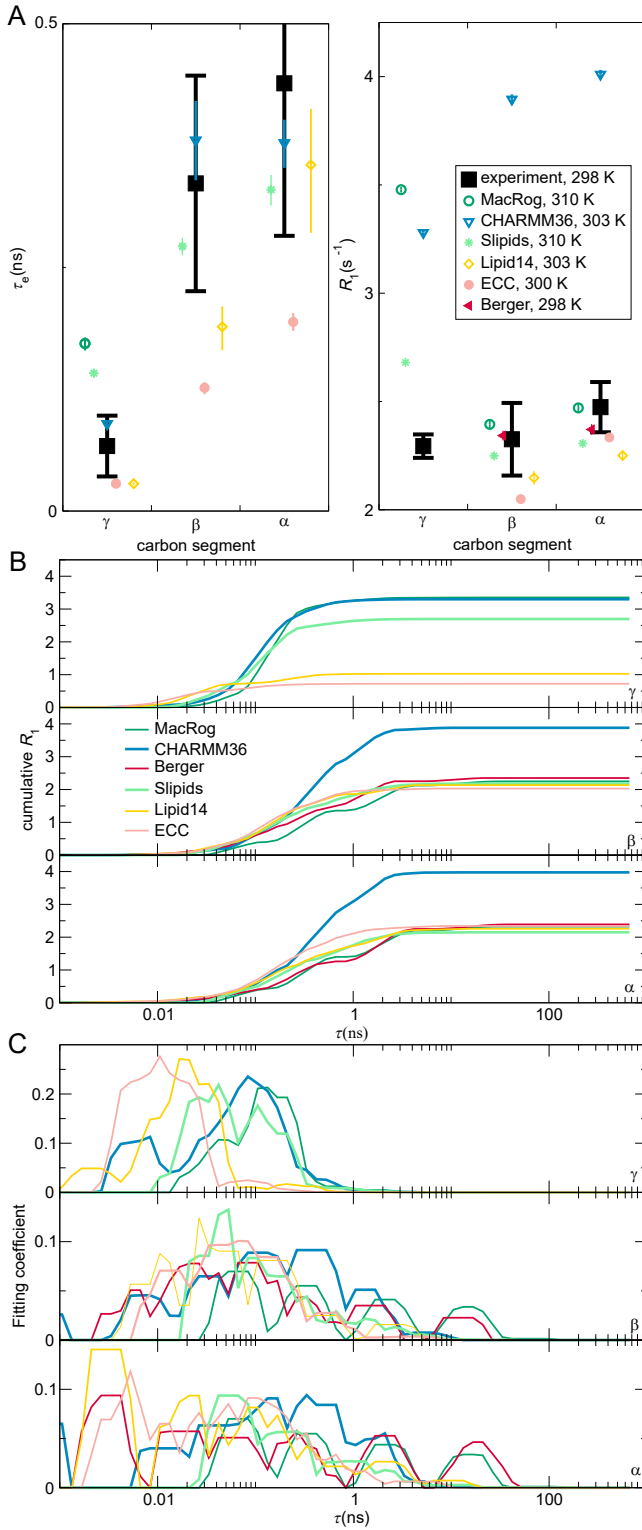


Figure 3: (A) Zoom on the headgroup τ_e (left panel) and R_1 (right). (B) 'Cumulative' R_1 (see Methods for definition) of the γ (top panel), β (middle), and α (bottom) segments. (C) Prefactor weights α_i from Eq. (10) of γ (top), β (middle), and α (bottom). In B and C, a sliding average over 5 neighboring data points is shown.

the non-zero weights occur, the smaller is the resulting R_1 .

For the β and α segments, Fig. 3B shows that the main contribution to R_1 rates arises from processes between 200 ps and 2 ns. As CHARMM36 has the largest weights of all models in this window (Fig. 3C), it overestimates R_1 . In contrast, Slipids, which has simultaneously R_1 and τ_e correct, has its largest weights at $\tau < 200$ ps. Indeed, considerable weights at short time scales (< 10 ps in α for Lipid14, ECC, Berger) and at long time scales (> 10 ns in both β and α for MacRog and Berger) do not manifest at all in the R_1 rates. However, the latter contribute heavily on τ_e , which is thus considerably overestimated by MacRog and Berger (Fig. 2).

What are the motions in the 0.2–2 ns window that are over-presented in CHARMM36? Identifying them and speeding them up would improve the model dynamics. However, the connection between the fitted correlation times and the correlation times of distinct motional processes, such as dihedral rotations and lipid wobbling, turns out to be highly non-trivial; we thus refrain from further analysis here.

Effect of cholesterol.

The experimental effective correlation times τ_e (Fig. 4A, top panels) show that when cholesterol is added, the glycerol region conformational dynamics slow down markedly. The tail segments slow down too, the effect increasing towards the backbone.

In stark contrast, however, the τ_e of head-group segments (γ , β , α) are unaffected by cholesterol. Furthermore, cholesterol induces no measurable change in the headgroup β and α segment dynamics at short (~ 1 ns) time scales, as demonstrated by the experimental R_1 rates (Fig. 4A, lower panels). That said, there is a small but measurable impact on R_1 at γ .

All the force fields investigated qualitatively reproduce the increase in τ_e (see Fig. 4B): Slipids gives the best magnitude estimates, while CHARMM36 and MacRog clearly overestimate the changes at the glycerol, C2, and C3 carbons. Notably, MacRog [11](#) and Berger?

erroneously predict slow down also for the β and α carbons, for which experiments detect no change. Note that, while CHARMM36 correctly shows no change in τ_e of the γ , β , and α carbons, it predicts a non-zero ΔR_1 for all three, indicating some inaccuracies in the headgroup rotational dynamics. Such inaccuracies might be reflected in the recent findings⁹⁰ (obtained using CHARMM36) that the headgroups of PCs neighbouring a cholesterol (within 6.6 Å) spend more time on top of the cholesterol than elsewhere; such arrested rotations could manifest on τ_e and R_1 . Interestingly, the tail ΔR_1 seem to be pretty well reproduced by all three all-atom force fields, whereas Berger fails to capture the change at the oleoyl double bond.

Effect of drying.

Figure 5A shows how a mild dehydration affects C–H bond dynamics in the PC headgroup and glycerol backbone; the plot compares the experimental effective correlation times τ_e measured for POPC at full hydration and for DMPC (1,2-dimyristoyl-sn-glycero-3-phosphocholine) at 13 waters per lipid.

The τ_e are the same within experimental accuracy, which suggests two conclusions. Firstly, the headgroup (γ , β , α) τ_e are unaffected by structural differences in the tails. This is analogous to what was seen experimentally when adding cholesterol (Fig. 4): Changes in the tail and glycerol regions do not reflect to the headgroup. Secondly, a mild dehydration does not alter the τ_e in the headgroup and glycerol regions.

Figure 5B shows the effects of dehydration in three MD models. Combination of the unrealistically slow dynamics, especially in the glycerol backbone, (Fig. 2) and the relatively short lengths of the openly available trajectories (Table 3) led to large uncertainty estimates. However, in the γ segment there is clearly no effect above 13 w/l in CHARMM36 and MacRog, in agreement with the experiments; reducing water content further induces a slow down, especially in MacRog below 10 w/l. Similarly, the β and α segments show no detectable change above 13 w/l for CHARMM36

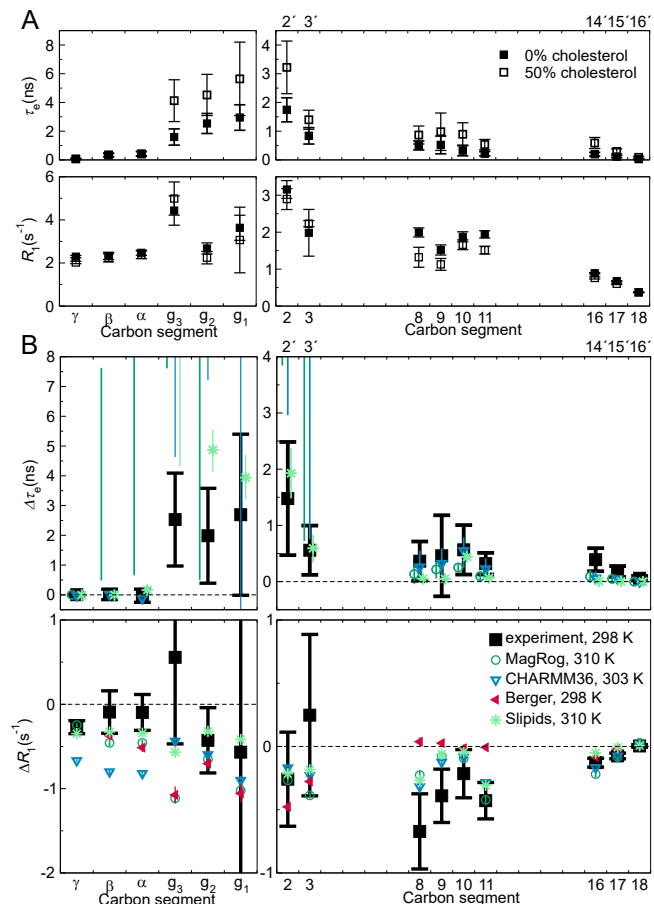


Figure 4: Effect of bilayer cholesterol content. (A) The experimental effective correlation times τ_e (top panels) and R_1 rates (bottom) in a pure POPC bilayer and in a bilayer containing 50% cholesterol. The data were measured at 298 K and full hydration. (B) The change in τ_e ($\Delta\tau_e$, top panels) and R_1 (ΔR_1 , bottom), both in experiments and in MD simulations, when bilayer composition changes from pure POPC to 50% cholesterol. Berger not shown for $\Delta\tau_e$, because the open data available were insufficient to determine meaningful error estimates. Error estimates for the simulated $\Delta\tau_e$ are the maximal possible based on the errors at 0% and 50% cholesterol; for other data regular error propagation is used. Table 2 provides further simulation details; for segment labeling, see Fig. 2.

12.@Hanne: Double check that the calculation of errors in (B) was as the caption describes. 13.Check if cholesterol data is in full hydration

and Berger, in agreement with the experiments; below 10 w/l Berger exhibits a slowdown, and in CHARMM36 the slowdown manifests as an abrupt increase of the uncertainty estimate.

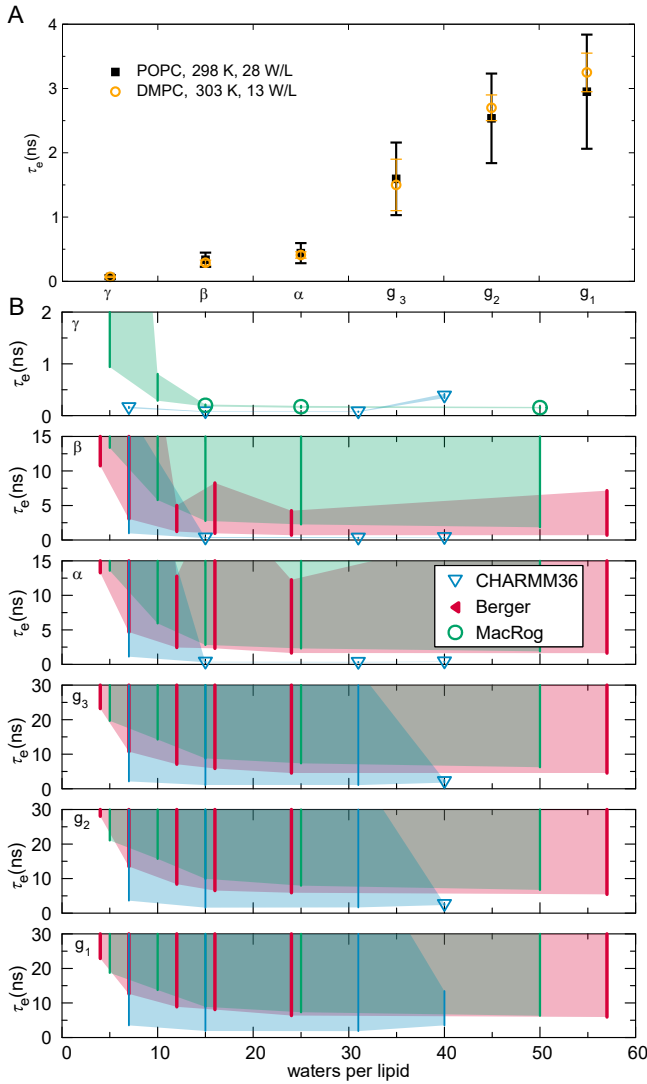


Figure 5: Effect of drying on effective correlation times in headgroup and glycerol backbone. (A) Experimental τ_e for DMPC (from Ref. 42) at low hydration do not significantly differ from the τ_e for POPC at full hydration. (B) Calculated τ_e for POPC at decreasing hydration in three MD models. Note that three Berger data points are from DLPC bilayers **dashed**. Symbols give the mean of segment hydrogens, if τ_e could be determined for all hydrogens; else only the error bar (extending from the mean of the lower to the mean of the upper uncertainty estimates) is shown; the area delimited by the error bars is shaded for visualization. See Table 3 for simulation details.

14.How to refer to full hydration POPC data?

15.Add also the black and orange (i.e. experimental) data points to B. 16.DLPC Berger points dashed or just in caption

Owing to the large uncertainties, we only point out the qualitative trends of the lower error estimates on the glycerol segments. For CHARMM36 it stays almost constant all the way until 7 w/l, for Berger and MacRog the lower error estimate suggests a retardation of the dynamics starting already from ~ 20 w/l.

These simulational findings suggest that experiments reducing hydration levels below 10 w/l would also show an increase in τ_e . This prediction is in line with the exponential slow-down of the headgroup conformational dynamics upon dehydration that was indicated by ^2H -NMR R_1 measurements of DOPC bilayers: $R_1 \sim \exp(-n_{w/l}/4)$.⁹¹ The slowdown was attributed to the reduction in the effective volume available for the headgroup⁹¹ owing to its tilt towards the membrane upon dehydration; the tilt is observed via changes of the lipid headgroup order parameters,⁹² and is qualitatively reproduced by all the simulation models.³²

Figure 6 shows a collection of experimental ^{13}C -NMR R_1 rates measured at 125 MHz for the headgroup segments at different water contents; in addition to the full hydration POPC data from Fig. 2, DMPC at 13 w/l,⁴² and POPC at 20 and 5 w/l⁴³ are shown. An increasing trend with decreasing hydration is observed for all the segments, indicating changes of headgroup dynamics at short (~ 1 ns) time scales. Interestingly, only CHARMM36 captures this, whereas Berger and MacRog give decreasing R_1 rates for β and α .

The slow down discussed here is of significance not only when simulating a bilayer (stack) under low hydration, but also for studies of intermembrane interactions, such as membrane fusion, because these naturally lead to dehydrated conditions when the lipid assemblies approach. Slower dynamics imply that longer simulation times are needed for equilibration, for reliably quantifying the properties of the bilayers, and for observing rare events.

Effect of cation binding.

18.MARKUS: I have started to think that we maybe should drop this section, because we do not have any experimental data to compare against. However, if we do

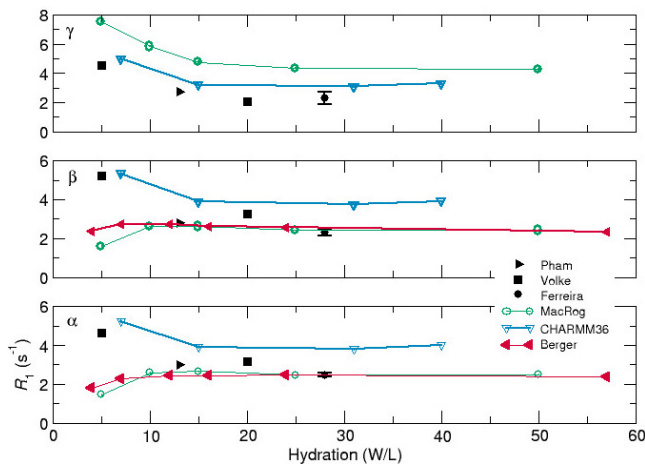


Figure 6: Effect of drying on ^{13}C -NMR R_1 rates of the headgroup segments (at 125 MHz) in experiments and simulations.

17.HA: Redo & merge this with the Fig. 5

decide to keep it, to me it seems that our main point here is not on the effects monovalent salt, but rather on the effects of cation binding. Therefore, it would be better to plot $\Delta\tau_e$ as a function of the bound cation charge, as we did in Fig. 3 of Ref. 33; then we could also include calcium data.

Finally, we comment on the response of the MD model dynamics to increasing amounts of monovalent salt. To our knowledge, no experimental ^{13}C -NMR R_1 or τ_e data exists as a function of monovalent salt concentration; therefore, the following discussion is kept qualitative. Experimentally, the modulation of α and β carbon order parameters upon increasing ion concentration have been used to quantify ion binding to lipid bilayers (the molecular electrometer^{33,93}). The order parameters are constant for POPC bilayers under NaCl addition in experiments, indicating negligible ion binding. Based on this, we anticipate the effective correlation times also to be unaffected by monovalent salt.

The molecular electrometer has been used to show that most molecular dynamics force fields overestimate the binding of monovalent ions to PC bilayers:³³ In the simulations the modulation of the α and β carbon order parameters by increasing NaCl concentration was overestimated compared to the experiments, and accompanied by accumulation of ions at the bilayer surface. In Fig. 7 we compare three force fields, one that is known to exhibit pro-

nounced overbinding³³ (MacRog) and two producing more realistic binding affinity (Slipids and CHARMM36). The lateral distribution of Na^+ ions near the bilayer is quantified in Fig. 7A whereas Fig. 7B shows the change in τ_e for increasing salt concentration. Ion accumulation results in a slow down in the effective correlation time. Correlation times extracted from CHARMM36 vary only a little (low ion binding) when ion concentration is increased, whereas a slightly more pronounced change is observed with Slipids, and MacRog exhibits a clear slow-down (significant ion binding). This indicates that, similarly to the order parameters, τ_e may be useful in investigating the ion binding affinity of lipid bilayers and experimental work exploring this avenue would be interesting.

19.validity of statement regarding Slipids

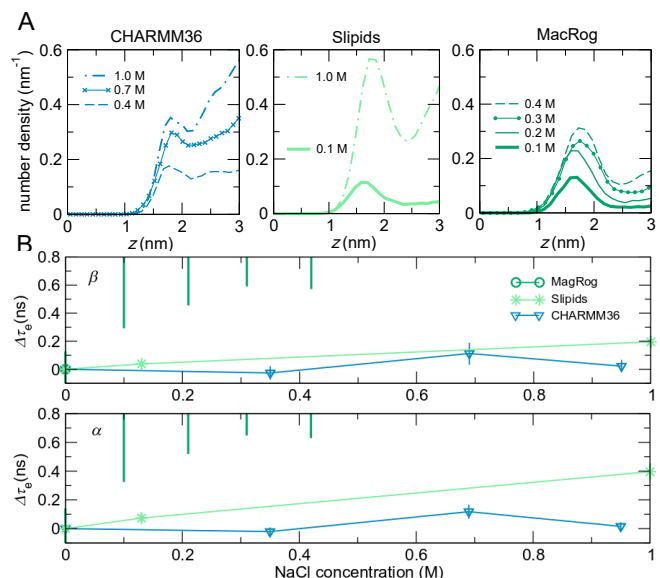


Figure 7: The impact of increasing ionic strength on effective correlation times. a) The density distribution (average over both leaflets) of Na^+ ions as function of distance z from the bilayer center. The plots for each force field are presented from left to right in the order of increasing ion accumulation. b) Effective correlation times for α and β C-H bonds in growing NaCl concentration from CHARMM36, Slipids, MacRog POPC simulations. Details on the simulation data are provided in Table 4.

Correlation time of S_{CH} versus τ_e .

To determine the C–H bond order parameter S_{CH} (Eq. (4)) in MD, one first calculates an instantaneous order parameter

$$S_{\text{CH}}(t) = \frac{1}{2} (3 \cos^2 \theta(t) - 1), \quad (13)$$

where $\theta(t)$ is the angle between the C–H bond and the membrane normal at time t . As this quantity is sampled along the trajectory, its average $\langle S_{\text{CH}}(t) \rangle$ approaches S_{CH} . For reliable determination of S_{CH} , it would be of interest to know the correlation time of this relaxation, because it determines the minimum simulation length required.

To this end, it is also of interest to know how this correlation time relates to τ_e . As discussed (see Fig. 1), in a bilayer the C–H bond’s second order rotational correlation function $g(\tau)$, see Eq. (2), approaches S_{CH}^2 with time. The speed of this approach tells how fast the C–H bond orientations are sampled. However, the correlation time of S_{CH} , which is calculated using the *a priori* knowledge of the membrane normal direction (Eq. (13)), does not need to equal τ_e . Rather, one would intuitively expect it to be shorter than τ_e , because the rotational averaging around the membrane normal direction is already implicitly taken into account in Eq. (13).

A further complication is that the relaxational process of the C–H bond direction (used to determine τ_e) can be single or multi-exponential. If the relaxation is single-exponential, τ_e is the relaxation time of this exponential process. If the relaxation is multi-exponential, τ_e is the weighted mean of the corresponding set of relaxation times, and it is a bit hard to say just based on τ_e how long one needs to sample to reach the S_{CH} , because this depends also on the weights of the processes.

Figure ?? shows this correlation for systems studied in this work; we see. . . **20.Laske bilayerissa S_{CH} :n korrelaatioaika (yksittäisessä lipidissa) vs τ_e . Tee scatter plot.**

4 Conclusions

Open access databanks of MD trajectories enables the creation new scientific information without running a single new simulation. Here, we demonstrated this by investigating the dynamics of a wide range of phosphatidylcholine molecular dynamics models using the existing trajectories from the NMRlipids databank.

We found that MD qualitatively captures the ^{13}C -NMR effective correlation time (τ_e) profile of POPC—the slow glycerol backbone and the faster motions of the headgroup and tail regions—but most MD force fields are prone to too slow dynamics of the glycerol C–H bonds (Fig. 2). While no force field reproduces all the experimental data, CHARMM36 and Slipids have an overall impressive τ_e . This is particularly true for CHARMM36, as it is also known to well reproduce the experimental conformational ensemble.³² That said, we find that CHARMM36 struggles with the balance of dynamics in the headgroup region: The R_1 rates, sensitive for ~ 1 -ns processes, are too high for the γ , β , and α segments (Fig. 3).

21.Make the point that the 500-ns simulations indicated by Vogel⁸⁹ are not needed for sufficient sampling?

In addition to standard conditions, we explored how the dynamics react to addition of cholesterol or NaCl, or to removal of water. MD qualitatively captures that when cholesterol is mixed into a POPC bilayer, the conformational dynamics in the tail and glycerol regions slows down; however, some force fields predict an (erroneous) slowdown also for the headgroup (Fig. 4). With increasing NaCl concentration, a behaviour reminiscent of the molecular electrometer was observed: Amount of ion binding to the bilayer correlated with the magnitude increase in τ_e ; this could open up the possibility of using τ_e in quantifying cation binding to lipid bilayers. When reducing the water content, MD exhibits slowdown of headgroup and backbone dynamics below ~ 10 waters per lipid in qualitative agreement with experimental data. **22.**

Hydration needs some kind of statement of significance.

By gathering a set of ^{13}C -NMR data on the phosphatidylcholine dynamics and charting the typical features of the existing MD models

against it, this study lays the foundation for further improvement of the force fields. While work is still needed in capturing even the correct conformations,³² realistic dynamics will be an essential part of developing MD into a true computational microscope.

Importantly, this work demonstrates the power of open data in creating new knowledge out of existing trajectories at a reduced computational and labor cost. If the data are well indexed and documented, this process could be automated and has the potential to facilitate faster progress, e.g., in the development of MD force fields, for example through machine learning approaches.

Acknowledgement

This material is based upon work supported by XXX under Grant No. XXX. The project is/isn't part of the NMRlipids open collaboration (nmrlipids.blogspot.fi)

References

- (1) Crystallography: Protein Data Bank. *Nat. New Biol.* **1971**, *233*, 223.
- (2) wwPDB consortium, Protein Data Bank: the single global archive for 3D macromolecular structure data. *Nucleic Acids Res.* **2019**, *47*, D520–D528.
- (3) Jordan, E.; Carrico, C. DNA Database. *Science* **1982**, *218*, 108.
- (4) Sayers, E. W.; Cavanaugh, M.; Clark, K.; Ostell, J.; Pruitt, K. D.; Karsch-Mizrachi, I. GenBank. *Nucleic Acids Res.* **2020**, *48*, D84–D86.
- (5) Levitt, M. Growth of novel protein structural data. *Proceedings of the National Academy of Sciences* **2007**, *104*, 3183–3188.
- (6) Brzezinski, D.; Dauter, Z.; Minor, W.; Jaskolski, M. On the evolution of the quality of macromolecular models in the PDB. *The FEBS Journal* **2020**, *287*, 2685–2698.
- (7) Harris, D. J. Can you bank on GenBank? *Trends in Ecology & Evolution* **2003**, *18*, 317–319.
- (8) Steinegger, M.; Salzberg, S. L. Terminating contamination: large-scale search identifies more than 2,000,000 contaminated entries in GenBank. *Genome Biology* **2020**, *21*, 115.
- (9) Rigden, D. J.; Fernández, X. M. The 27th annual Nucleic Acids Research database issue and molecular biology database collection. *Nucleic Acids Research* **2020**, *48*, D1–D8.
- (10) Simpkin, A. J.; Thomas, J. M. H.; Simkovic, F.; Keegan, R. M.; Rigden, D. J. Molecular replacement using structure predictions from databases. *Acta Crystallographica Section D Structural Biology* **2019**, *D75*, 1051–1062.
- (11) Leelananda, S. P.; Lindert, S. Using NMR Chemical Shifts and Cryo-EM Density Restraints in Iterative Rosetta-MD Protein Structure Refinement. *Journal of Chemical Information and Modeling* **2020**, *60*, 2522–2532.
- (12) Senior, A. W. et al. Improved protein structure prediction using potentials from deep learning. *Nature* **2020**, *577*, 706–710.
- (13) Huang, P.-S.; Boyken, S. E.; Baker, D. The coming of age of de novo protein design. *Nature* **2016**, *537*, 320.
- (14) Westbrook, J. D.; Burley, S. K. How Structural Biologists and the Protein Data Bank Contributed to Recent FDA New Drug Approvals. *Structure* **2019**, *27*, 211–217.
- (15) Martinez-Mayorga, K.; Madariaga-Mazon, A.; Medina-Franco, J.; Maggiora, G. The impact of chemoinformatics on drug discovery in the pharmaceutical industry. *Expert Opinion on Drug Discovery* **2020**, *15*, 293–306.

- (16) Senderowitz, H.; Tropsha, A. Materials Informatics. *J. Chem. Inf. Model.* **2018**, *58*, 2377–2379.
- (17) Wan, X.; Feng, W.; Wang, Y.; Wang, H.; Zhang, X.; Deng, C.; Yang, N. Materials Discovery and Properties Prediction in Thermal Transport via Materials Informatics: A Mini Review. *Nano Letters* **2019**, *19*, 3387–3395.
- (18) Perez-Riverol, Y.; Zorin, A.; Dass, G.; Vu, M.-T.; Xu, P.; Glont, M.; Vizcaíno, J. A.; Jarnuczak, A. F.; Petryszak, R.; Ping, P.; Hermjakob, H. Quantifying the impact of public omics data. *Nature Communications* **2019**, *10*.
- (19) Feng, Z.; Verdigué, N.; Costanzo, L. D.; Goodsell, D. S.; Westbrook, J. D.; Burley, S. K.; Zardecki, C. Impact of the Protein Data Bank Across Scientific Disciplines. *Data Science Journal* **2020**, *19*, 25.
- (20) Feig, M.; Abdullah, M.; Johnsson, L.; Pettitt, B. M. Large scale distributed data repository: design of a molecular dynamics trajectory database. *Future Generation Computer Systems* **1999**, *16*, 101–110.
- (21) Tai, K.; Murdock, S.; Wu, B.; Ng, M. H.; Johnston, S.; Fangohr, H.; Cox, S. J.; Jeffreys, P.; Essex, J. W.; P. Sansom, M. S. BioSimGrid: towards a worldwide repository for biomolecular simulations. *Organic & Biomolecular Chemistry* **2004**, *2*, 3219–3221.
- (22) Silva, C. G.; Ostropevsky, V.; Loureiro-Ferreira, N.; Berrar, D.; Swain, M.; Dubitzky, W.; Brito, R. M. M. P-found: The Protein Folding and Unfolding Simulation Repository. 2006 IEEE Symposium on Computational Intelligence and Bioinformatics and Computational Biology. 2006; pp 1–8.
- (23) Hildebrand, P. W.; Rose, A. S.; Tieermann, J. K. S. Bringing Molecular Dynamics Simulation Data into View. *Trends in Biochemical Sciences* **2019**, *44*, 902–913.
- (24) Abraham, M. et al. Sharing Data from Molecular Simulations. *Journal of Chemical Information and Modeling* **2019**, *59*, 4093–4099.
- (25) Abriata, L. A.; Lepore, R.; Dal Peraro, M. About the need to make computational models of biological macromolecules available and discoverable. *Bioinformatics* **2020**, *36*, 2952–2954.
- (26) Hospital, A.; Battistini, F.; Soliva, R.; Gelpí, J. L.; Orozco, M. Surviving the deluge of biosimulation data. *WIREs Computational Molecular Science* **2020**, *10*, e1449.
- (27) Hospital, A.; Andrio, P.; Cugnasco, C.; Codo, L.; Becerra, Y.; Dans, P. D.; Battistini, F.; Torres, J.; Goñi, R.; Orozco, M.; Gelpí, J. L. BIGNASim: a NoSQL database structure and analysis portal for nucleic acids simulation data. *Nucleic Acids Research* **2016**, *44*, D272–D278.
- (28) Bekker, G.-J.; Kawabata, T.; Kurisu, G. The Biological Structure Model Archive (BSM-Arc): an archive for in silico models and simulations. *Biophysical Reviews* **2020**, *12*, 371–375.
- (29) Mixcoha, E.; Rosende, R.; Garcia-Fandino, R.; Piñeiro, Á. Cyclo-lib: a database of computational molecular dynamics simulations of cyclodextrins. *Bioinformatics* **2016**, *32*, 3371–3373.
- (30) Rodríguez-Espigares, I. et al. GPCRmd uncovers the dynamics of the 3D-GPCRome. *bioRxiv* **2019**, 839597.
- (31) Miettinen, M. S.; NMRlipids Collaboration; Ollila, O. H. S. LDB: Lipid Data-bank from the NMRlipids Project. *Biophysical Journal* **2019**, *116*, 91a.
- (32) Botan, A. et al. Toward Atomistic Resolution Structure of Phosphatidylcholine Headgroup and Glycerol Backbone at Different Ambient Conditions. *The Journal of Physical Chemistry B* **2015**, *119*, 15075–15088, PMID: 26509669.

- (33) Catte, A.; Girych, M.; Javanainen, M.; Loison, C.; Melcr, J.; Miettinen, M. S.; Monticelli, L.; Määttä, J.; Oganessian, V. S.; Ollila, O. H. S.; Tynkkynen, J.; Vilov, S. Molecular electrometer and binding of cations to phospholipid bilayers. *Phys. Chem. Chem. Phys.* **2016**, *18*, 32560–32569.
- (34) Antila, H.; Buslaev, P.; Favela-Rosales, F.; Ferreira, T. M.; Gushchin, I.; Javanainen, M.; Kav, B.; Madsen, J. J.; Melcr, J.; Miettinen, M. S.; Määttä, J.; Nencini, R.; Ollila, O. H. S.; Piggot, T. J. Headgroup Structure and Cation Binding in Phosphatidylserine Lipid Bilayers. *J. Phys. Chem. B* **2019**, *123*, 9066–9079.
- (35) Robustelli, P.; Piana, S.; Shaw, D. E. Developing a molecular dynamics force field for both folded and disordered protein states. *Proc. Natl. Acad. Sci.* **2018**, *115*, E4758–E4766.
- (36) Henriques, J.; Arleth, L.; Lindorff-Larsen, K.; Skepö, M. On the Calculation of SAXS Profiles of Folded and Intrinsically Disordered Proteins from Computer Simulations. *J. Mol. Biol.* **2018**, *430*, 2521–2539.
- (37) Virtanen, S. I.; Kiirikki, A. M.; Mikula, K. M.; Iwai, H.; Ollila, O. H. S. Heterogeneous dynamics in partially disordered proteins. *Phys. Chem. Chem. Phys.* **2020**, –.
- (38) Ollila, S.; Pabst, G. Atomistic resolution structure and dynamics of lipid bilayers in simulations and experiments. *BBA - Biomembranes* **2016**, *1858*, 2512–2528.
- (39) Antila, H. S.; Wurl, A.; Ollila, O. H. S.; Miettinen, M. S.; Ferreira, T. M. Quasi-uncoupled rotational diffusion of phospholipid headgroups from the main molecular frame. *arXiv preprint* **2020**, arXiv:2009.06774v1.
- (40) Han, J.; Pluhackova, K.; Böckmann, R. A. The Multifaceted Role of SNARE Proteins in Membrane Fusion. *Frontiers in Physiology* **2017**, *8*, 5.
- (41) Ferreira, T. M.; Ollila, O. H. S.; Pigliapochi, R.; Dabkowska, A. P.; Topgaard, D. Model-free estimation of the effective correlation time for C–H bond reorientation in amphiphilic bilayers: ^1H – ^{13}C solid-state NMR and MD simulations. *The Journal of Chemical Physics* **2015**, *142*, 044905.
- (42) Pham, Q. D.; Topgaard, D.; Sparr, E. Cyclic and Linear Monoterpenes in Phospholipid Membranes: Phase Behavior, Bilayer Structure, and Molecular Dynamics. *Langmuir* **2015**, *31*, 11067–11077, PMID: 26375869.
- (43) Volke, F.; Pampel, A. Membrane Hydration and Structure on a Subnanometer Scale as Seen by High Resolution Solid State Nuclear Magnetic Resonance: POPC and POPC/ C_{12}EO_4 Model Membranes. *Biophys. J.* **1995**, *68*, 1960–1965.
- (44) Feller, S. E.; Gawrisch, K.; MacKerell, A. D. Polyunsaturated Fatty Acids in Lipid Bilayers: Intrinsic and Environmental Contributions to Their Unique Physical Properties. *Journal of the American Chemical Society* **2002**, *124*, 318–326, PMID: 11782184.
- (45) Eldho, N. V.; Feller, S. E.; Tristram-Nagle, S.; Polozov, I. V.; Gawrisch, K. Polyunsaturated Docosahexaenoic vs Docosapentaenoic Acid Differences in Lipid Matrix Properties from the Loss of One Double Bond. *Journal of the American Chemical Society* **2003**, *125*, 6409–6421, PMID: 12785780.
- (46) Wohllert, J.; Edholm, O. Dynamics in atomistic simulations of phospholipid membranes: Nuclear magnetic resonance relaxation rates and lateral diffusion. *The Journal of Chemical Physics* **2006**, *125*, 204703.
- (47) Klauda, J. B.; Roberts, M. F.; Redfield, A. G.; Brooks, B. R.; Pastor, R. W.

- Rotation of Lipids in Membranes: Molecular Dynamics Simulation, 31P Spin-Lattice Relaxation, and Rigid-Body Dynamics. *Biophysical Journal* **2008**, *94*, 3074–3083.
- (48) Leftin, A.; Brown, M. F. An NMR database for simulations of membrane dynamics. *Biochimica et Biophysica Acta (BBA) - Biomembranes* **2011**, *1808*, 818 – 839, Including the Special Section: Protein translocation across or insertion into membranes.
- (49) Klauda, J. B.; Eldho, N. V.; Gawrisch, K.; Brooks, B. R.; Pastor, R. W. Collective and Noncollective Models of NMR Relaxation in Lipid Vesicles and Multilayers. *The Journal of Physical Chemistry B* **2008**, *112*, 5924–5929, PMID: 18179193.
- (50) Ollila, S.; Hyvönen, M. T.; Vattulainen, I. Polyunsaturation in Lipid Membranes: Dynamic Properties and Lateral Pressure Profiles. *J. Phys. Chem. B* **2007**, *111*, 3139–3150.
- (51) Ollila, O. H. S.; Ferreira, T.; Topgaard, D. MD simulation trajectory and related files for POPC bilayer (Berger model delivered by Tieleman, Gromacs 4.5). 2014; {<http://dx.doi.org/10.5281/zenodo.13279>}.
- (52) Klauda, J. B.; Venable, R. M.; Freites, J. A.; O'Connor, J. W.; Tobias, D. J.; Mondragon-Ramirez, C.; Vorobyov, I.; Jr, A. D. M.; Pastor, R. W. Update of the CHARMM All-Atom Additive Force Field for Lipids: Validation on Six Lipid Types. *J. Phys. Chem. B* **2010**, *114*, 7830–7843.
- (53) Santuz, H. MD simulation trajectory and related files for POPC bilayer (CHARMM36, Gromacs 4.5). 2015; <http://dx.doi.org/10.5281/zenodo.14066>, DOI: 10.5281/zenodo.14066.
- (54) Antila, H. . 2018; <http://dx.doi.org/10.5281/zenodo.148560>, DOI: 10.5281/zenodo.1468560.
- (55) Kulig, W.; Jurkiewicz, P.; Olżyńska, A.; Tynkkynen, J.; Javanainen, M.; Manna, M.; Rog, T.; Hof, M.; Vattulainen, I.; Jungwirth, P. Experimental determination and computational interpretation of biophysical properties of lipid bilayers enriched by cholesteryl hemisuccinate. *Biochim. Biophys. Acta* **2015**, *1848*, 422 – 432.
- (56) Javanainen, M. POPC/Cholesterol @ 310K. 0, 10, 40, 50 and 60 mol-cholesterol. Model by Maciejewski and Rog. **2015**,
- (57) Dickson, C. J.; Madej, B. D.; Skjevik, A. A.; Betz, R. M.; Teigen, K.; Gould, I. R.; Walker, R. C. Lipid14: The Amber Lipid Force Field. *J. Chem. Theory Comput.* **2014**, *10*, 865–879.
- (58) Ollila, O. H. S.; Retegan, M. MD simulation trajectory and related files for POPC bilayer (Lipid14, Gromacs 4.5). 2014; DOI: 10.5281/zenodo.12767.
- (59) Jämbeck, J. P. M.; Lyubartsev, A. P. An Extension and Further Validation of an All-Atomistic Force Field for Biological Membranes. *J. Chem. Theory Comput.* **2012**, *8*, 2938–2948.
- (60) Javanainen, M. POPC with 0, 10, 20, and 30 mol-Slipids force field. 2016; <http://dx.doi.org/10.5281/zenodo.3243328>.
- (61) Melcr, J.; Martinez-Seara, H.; Nencini, R.; Kolafa, J.; Jungwirth, P.; Ollila, O. H. S. Accurate Binding of Sodium and Calcium to a POPC Bilayer by Effective Inclusion of Electronic Polarization. *The Journal of Physical Chemistry B* **2018**, *122*, 4546–4557.
- (62) Melcr, J. Simulations of POPC lipid bilayer in water solution at various NaCl, KCl and CaCl₂ concentrations using ECC-POPC force field. **2019**,
- (63) Hölte, M.; Förster, T.; Brandt, B.; Engels, T.; von Rybinski, W.; Hölte, H.-D. Molecular dynamics simulations of stratum corneum lipid models: fatty acids and

- cholesterol. *Biochim. Biophys. Acta* **2001**, *1511*, 156 – 167.
- (64) Ferreira, T. M.; Coreta-Gomes, F.; Ollila, O. H. S.; Moreno, M. J.; Vaz, W. L. C.; Topgaard, D. Cholesterol and POPC segmental order parameters in lipid membranes: solid state 1H – 13C NMR and MD simulation studies. *Phys. Chem. Chem. Phys.* **2013**, *15*, 1976–1989.
- (65) Ollila, O. H. S. MD simulation trajectory and related files for POPC/cholesterol (50 molmodified Höltje, Gromacs 4.5). **2014**,
- (66) Lim, J. B.; Rogaski, B.; Klauda, J. B. Update of the Cholesterol Force Field Parameters in CHARMM. *J. Phys. Chem. B* **2012**, *116*, 203–210.
- (67) Santuz, H. MD simulation trajectory for POPC/50% Chol bilayer (CHARMM36, Gromacs 4.5). 2015; <http://dx.doi.org/10.5281/zenodo.14068>, DOI: 10.5281/zenodo.14068.
- (68) Jämbeck, J. P. M.; Lyubartsev, A. P. Another Piece of the Membrane Puzzle: Extending Slipids Further. *Journal of Chemical Theory and Computation* **2013**, *9*, 774–784, PMID: 26589070.
- (69) Kanduc, M.; Schneck, E.; Netz, R. R. Hydration Interaction between Phospholipid Membranes: Insight into Different Measurement Ensembles from Atomistic Molecular Dynamics Simulations. *Langmuir* **2013**, *29*, 9126–9137.
- (70) Kanduc, M. MD trajectory for DLPC bilayer (Berger, Gromacs 4.5.4), nw=24 w/l. 2015; DOI: 10.5281/zenodo.16289.
- (71) Kanduc, M. MD trajectory for DLPC bilayer (Berger, Gromacs 4.5.4), nw=16 w/l. 2015; DOI: 10.5281/zenodo.16292.
- (72) Kanduc, M. MD trajectory for DLPC bilayer (Berger, Gromacs 4.5.4), nw=12 w/l. 2015; DOI: 10.5281/zenodo.16293.
- (73) Ollila, O. H. S. MD simulation trajectory and related files for POPC bilayer in low hydration (Berger model delivered by Tieleman, Gromacs 4.5). **2015**,
- (74) Kanduc, M. MD trajectory for DLPC bilayer (Berger, Gromacs 4.5.4), nw=4 w/l. 2015; DOI: 10.5281/zenodo.16295.
- (75) Ollila, O. H. S.; Miettinen, M. MD simulation trajectory and related files for POPC bilayer in medium low hydration (CHARMM36, Gromacs 4.5). 2015; <http://dx.doi.org/10.5281/zenodo.13946>, DOI: 10.5281/zenodo.13946.
- (76) Ollila, O. H. S.; Miettinen, M. MD simulation trajectory and related files for POPC bilayer in low hydration (CHARMM36, Gromacs 4.5). 2015; <http://dx.doi.org/10.5281/zenodo.13945>, DOI: 10.5281/zenodo.13945.
- (77) Javanainen, M. POPC @ 310K, varying water-to-lipid ratio. Model by Maciejewski and Rog. 2014; <http://dx.doi.org/10.5281/zenodo.13498>, DOI: 10.5281/zenodo.13498.
- (78) Venable, R. M.; Luo, Y.; Gawrisch, K.; Roux, B.; Pastor, R. W. Simulations of Anionic Lipid Membranes: Development of Interaction-Specific Ion Parameters and Validation Using NMR Data. *J. Phys. Chem. B* **2013**, *117*, 10183–10192.
- (79) Ollila, O. H. S. MD simulation trajectory and related files for POPC bilayer with 350mM NaCl (CHARMM36, Gromacs 4.5). 2015; <http://dx.doi.org/10.5281/zenodo.32496>.
- (80) Ollila, O. H. S. MD simulation trajectory and related files for POPC bilayer with 690mM NaCl (CHARMM36, Gromacs 4.5). 2015; <http://dx.doi.org/10.5281/zenodo.32497>.
- (81) Ollila, O. H. S. MD simulation trajectory and related files for POPC bilayer

- with 950mM NaCl (CHARMM36, Gromacs 4.5). 2015; <http://dx.doi.org/10.5281/zenodo.32498>.
- (82) Åqvist, J. Ion-water interaction potentials derived from free energy perturbation simulations. *J. Phys. Chem.* **1990**, *94*, 8021–8024.
 - (83) Javanainen, M.; Tynkkynen, J. POPC @ 310K, varying amounts of NaCl. Model by Maciejewski and Rog. 2015; <http://dx.doi.org/10.5281/zenodo.14976>.
 - (84) Smith, D. E.; Dang, L. X. Computer simulations of NaCl association in polarizable water. *J. Chem. Phys* **1994**, *100*, 3757–3766.
 - (85) Javanainen, M. POPC @ 310K, 130 mM of NaCl. Slipids with ions by Smith & Dang. 2015; <http://dx.doi.org/10.5281/zenodo.35275>.
 - (86) Javanainen, M. POPC with varying amounts of cholesterol, 1 M of NaCl. Slipids with ions by Smith & Dang. 2015; <http://dx.doi.org/10.5281/zenodo.259341>.
 - (87) Schlenkrich, M.; Brickmann, J.; MacKerell, A. D.; Karplus, M. *Biological Membranes*; Springer, 1996; pp 31–81.
 - (88) Feller, S. E.; MacKerell, A. D. An improved empirical potential energy function for molecular simulations of phospholipids. *The Journal of Physical Chemistry B* **2000**, *104*, 7510–7515.
 - (89) Vogel, A.; Feller, S. E. Headgroup Conformations of Phospholipids from Molecular Dynamics Simulation: Sampling Challenges and Comparison to Experiment. *The Journal of Membrane Biology* **2012**, *245*, 23–28.
 - (90) Leeb, F.; Maibaum, L. Spatially Resolving the Condensing Effect of Cholesterol in Lipid Bilayers. *Biophysical Journal* **2018**, *115*, 2179 – 2188.
 - (91) Ulrich, A.; Watts, A. Molecular response of the lipid headgroup to bilayer hydration monitored by 2H-NMR. *Biophys. J.* **1994**, *66*, 1441 – 1449.
 - (92) Bechinger, B.; Seelig, J. Conformational changes of the phosphatidylcholine headgroup due to membrane dehydration. A 2H-NMR study. *Chemistry and Physics of Lipids* **1991**, *58*, 1 – 5.
 - (93) Seelig, J.; MacDonald, P. M.; Scherer, P. G. Phospholipid head groups as sensors of electric charge in membranes. *Biochemistry* **1987**, *26*, 7535–7541, PMID: 3322401.

Graphical TOC Entry

TOC here if needed